Materials Today Communications 49 (2025) 114274

Contents lists available at ScienceDirect

Materials Today Communications

journal homepage: www.elsevier.com/locate/mtcomm

# Carburization-assisted conversion of N-doped Mo to N-doped $Mo_2C$ for efficient electrocatalytic hydrogen evolution

Stefanos Chaitoglou [a,b,*], Subrata Ghosh [c,d,**], Shubhadeep Majumdar [a,b], Roger Amade-Rovira [a,b], Carlo S. Casari [c], Enric Bertran-Serra [a,b]

[a] Department of Applied Physics, University of Barcelona, C/Martí i Franques, 1, Barcelona, Catalunya 08028, Spain
[b] ENPHOCAMAT Group, Institute of Nanoscience and Nanotechnology (IN2UB), University of Barcelona, C/ Martí i Franques, 1, Barcelona, Catalunya 08028, Spain
[c] Micro and Nanostructured Materials Laboratory — NanoLab, Department of Energy, Politecnico di Milano, via Lambruschini, Milano 20156, Italy
[d] Faculty of Mechatronics, Warsaw University of Technology, sw. Andrzeja Boboli 8, Warsaw 02-525, Poland

ARTICLE INFO

*Keywords:*
Molybdenum carbide
Pulsed-laser deposition
Hydrogen evolution
High-temperature carburization

ABSTRACT

Advanced nanomaterials hold promise in accelerating electrocatalytic reactions, especially with respect to the hydrogen evolution reaction (HER). Their activity can be enhanced by engineering both intrinsic efficiency and surface features at the micro/nano scale. Here, we demonstrate a carburization-assisted chemical conversion of amorphous N-doped Mo film into crystallized N-doped $Mo_2C$ film via high-temperature annealing in a $CH_4$ gas environment. The benefits of this process become evident when comparing the electrocatalytic efficiency of the pristine and annealed composites toward HER. The carbon substrate and $CH_4$ gas act as carbon sources, enabling Mo carburization during annealing due to the migration of carbon from the substrate and its reaction with the overlying metal. This phenomenon is verified by high-temperature annealing of N-doped Mo grown on a Si substrate under an inert gas environment. The columnar growth—an intrinsic feature of pulsed-laser deposition—enables the formation of a nanocomposite with an enhanced surface area. N-doped $Mo_2C$ shows a low overpotential of −192 mV at 10 mA/cm$^2$, making it one of the best-performing $Mo_2C$ thin films. This work offers a simple strategy for the preparation of N-doped nanostructured $Mo_2C$ and provides insights into the high-temperature annealing of transition metals on carbon supports, which can be useful for applications in the energy sector.

## 1. Introduction

The concept of the hydrogen economy refers to the development of an energy system in which hydrogen replaces fossil fuels as the primary energy carrier. Hydrogen is considered a clean and sustainable energy source because it produces only electricity and water in fuel cells. Therefore, it is expected to play a key role in the decarbonization of society [1].

Water electrolysis uses electricity to split the water into hydrogen and oxygen. Hydrogen produced via water electrolysis is referred to as green hydrogen because it is generated using renewable energy sources, resulting in minimal or zero carbon emissions. In an electrolysis cell, hydrogen is produced at the cathode via the hydrogen evolution reaction (HER). Theoretically, HER requires no overpotential to proceed. Nevertheless, due to sluggish reaction kinetics, overpotentials are typically required to drive the reaction.

Currently, significant efforts are focused on the development of electrocatalysts that can drive HER at minimal overpotentials. Although Pt and other Pt-like noble metals remain the most efficient electrocatalysts, their high cost and scarcity hinder their application in industrial-scale electrolyzers [2]. As a result, the development of advanced electrocatalysts based on more abundant elements has become an urgent priority.

Among these alternatives, transition metals such as molybdenum (Mo) have attracted considerable attention for HER applications. According to Trasatti's volcano plot, the energy required for Mo to form a hydrogen-metal bond is comparable to that of noble metals [3]. Moreover, Mo and its compounds are relatively stable under harsh, acidic

* Corresponding author at: Department of Applied Physics, University of Barcelona, C/Martí i Franques, 1, Barcelona, Catalunya 08028, Spain.
** Corresponding author at: Micro and Nanostructured Materials Laboratory — NanoLab, Department of Energy, Politecnico di Milano, via Lambruschini, Milano 20156, Italy.
*E-mail addresses:* stefanoschaitoglou@ub.edu (S. Chaitoglou), subrata.ghosh@pw.edu.pl (S. Ghosh).

https://doi.org/10.1016/j.mtcomm.2025.114274
Received 21 July 2025; Received in revised form 22 September 2025; Accepted 6 November 2025
Available online 7 November 2025

conditions, making them suitable candidates for use in proton-exchange membrane (PEM) cells. Additionally, Mo can form stable carbide phases, which have demonstrated high efficiency toward HER. This efficiency arises from their favorable electronic structure: the formation of metal–carbon bonds modifies the transition metal *d*-band, making it resemble the electronic structure of Pt [4].

Various experimental studies have confirmed the effectiveness of $Mo_2C$ composites for HER [5–7]. $Mo_2C$ can be synthesized via both chemical and physical methods. While chemical approaches are typically used to synthesize nanocrystals, physical methods are better suited for depositing robust and homogeneous thin films [8,9]. Furthermore, nitrogen (N) doping has emerged as a promising strategy to enhance the HER activity of $Mo_2C$. N-doping can: i) enhance the electronic structure of $Mo_2C$, facilitating rapid adsorption/desorption of hydrogen intermediates ($H_{ads}$) [10]; ii) increase the structural disorder and interlayer spacing, thereby exposing more catalytically active sites [11]; and iii) strengthen the Mo–C bonds, which can improve electron transport [12].

Traditionally, nitrogen doping is achieved via harsh and potentially hazardous $NH_3$ treatments, either during growth or post-deposition [13]. Therefore, developing N-doped Mo-based materials without relying on $NH_3$ is of significant interest.

In the present work, Mo thin films were deposited via pulsed-laser deposition (PLD) onto carbon paper in a nitrogen-rich atmosphere. The samples were then subjected to high-temperature annealing in a methane/argon atmosphere to induce crystallization and carburization. Our results demonstrate that carburization can occur through both the carbon-rich gas phase and the carbon-based substrate. The resulting composites were evaluated as working electrodes for HER, and the obtained outcome confirms the superior performance of the carbide phase compared to the pristine metallic Mo. Unlike conventional methods that require toxic $NH_3$ or external carbon sources, our approach enables *in-situ* carburization using a carbon substrate, offering a safer and more efficient synthesis route.

## 2. Experimental part

### 2.1. Deposition of thin films

Amorphous N-doped Mo columnar compact film was synthesized using PLD at room temperature. The detail of deposition is already reported in our previous publication [14]. Briefly, PLD (second harmonic Q-switched Nd:YAG laser with a wavelength of 532 nm) with pulse duration of 5–7 nanosecond pulse, a repetition rate of 10 Hz and a fluence of 10.6 J/cm$^2$), was used to ablate 2-inch Mo-target (99.99 % purity, purchased from Testbourne B. V.) in a stainless-steel vacuum chamber under the high pure $N_2$ (5 N purity) environment. At the beginning, the chamber was evacuated down to $2 \times 10^{-3}$ Pa base pressure using a primary scroll pump and turbo-molecular pump. The Mo-target was placed on a rotating/translating holder for uniform ablation, and the Si (100) and carbon paper substrates were placed on the rotating substrate holder for uniform deposition. The distance between the target and substrate of 5 cm was maintained throughout the deposition. The deposition pressure of $1.5 \times 10^{-2}$ Pa was maintained for the first 3 min to obtain a very compact film, and the pressure was 300 Pa for the next phase of deposition to obtain a columnar structure. Finally, the laser and then the pump were turned off, the chamber was vented, and the samples were taken out for further studies.

### 2.2. High-temperature annealing

Pristine samples were introduced into an oven consisting of a quartz tube. A graphite piece was used as a sample holder. Upon introduction of the sample in the centre of the tube, the chamber was evacuated with a turbomolecular pump at a background pressure of $8 \times 10^{-4}$ Pa. The tubular furnace was heated up to 950 °C. 10 sccm of Ar were introduced in the chamber during the heating, while the pressure remained constant at 1 Pa, with the assistance of a rotatory valve. The annealing step lasts for 30 min under 10 sccm of Ar gas environment. For annealing in a $CH_4$ atmosphere, 10 sccm of $CH_4$ was introduced in the chamber, while the flow of Ar carrier gas was maintained. Finally, the oven was let to cool to room temperature, while Ar gas flow was maintained (Fig. S1).

### 2.3. Structural and chemical characterization

The morphology of pristine and annealed samples was characterized via scanning electron microscopy (SEM), made using the FESEM JEOL JSM-7001F at 20 kV. Energy-dispersive X-ray spectroscopy (EDS) was employed to determine the elemental composition of the samples. XRD analysis was carried out using the Anton Paar XRDynamic 500 multipurpose powder diffractometer in Bragg-Brentano mode with a 360 mm radius. The sample was exposed to Cu $K_\alpha$(1 +2) radiation with a length of 1.5418 Å, and $2\theta/\theta$ scans were conducted from 4° to 100°, with 2θ step size of 0.02°, and each measurement step lasted for 30 s. XPS analysis was performed with the PHI 5500 Multi-Technique System (from Physical Electronics, Chanhassen, MN, USA) using a monochromatic X-Ray source (Al Kα line of 1486.6 eV and 350 W. The area analysed had a diameter of 0.8 mm, with Survey XPS spectra having a pass energy of 187.5 eV and 0.8 eV/step, and elemental spectra having a pass energy of 11.75 eV and 0.1 eV/step. Raman spectroscopy was employed to further study the molybdenum carbide on carbon nanotubes, revealing the vibrational modes of all studied films. The Raman microscope used was HR800, Lab-Ram (HORIBA France SAS, Palaiseau, France), equipped with a 532 nm solid-state laser, operating at a power of 5 mW with an irradiation area diameter of 1 μm.

### 2.4. Electrochemical characterization

The electrochemical behaviour of the sample was investigated for HER using a potentiostat/galvanostat (GAMRY INSTRUMENTS, Interface 1010.). The experiments were conducted using a 3-electrode system at room temperature. An Ag/AgCl electrode with an internal 3 M KCl solution served as the reference electrode, while a piece of graphite felt was utilized as the counter electrode. The samples under study constituted the working electrode, which was connected to the power supply using a crocodile clip. The sample was cut to achieve a surface area of 1 cm$^2$. Linear sweep voltammetry was performed with a scan rate of 10 mVs$^{-1}$ using a 1 M $H_2SO_4$ electrolyte. Chronoamperometry tests were performed to assess the electrode endurance, using a constant bias of −290 mV. The charge transfer resistance was evaluated via electrochemical impedance spectroscopy (EIS) across a frequency range from 100 kHz to 0.1 Hz, while employing an *a.c.* potential of 10 mV and a *d.c.* potential of −500 mV *vs* reference electrode. Cyclic voltammetry (CV) was performed in the non-Faradaic voltage window of 0 −0.2 V, where the compounds are electrochemically inactive, at a scan rate ($r_{sc}$) of 10 −200 mV/s. Capacitances were calculated from the slope of the straight line fit of the curve of $I_{max}$ versus scan rates since

$$I = \frac{dQ}{dt} = \frac{dQ}{dV} \quad r_{sc} = C \quad r_{sc}$$

All potentials were converted against the RHE using the Nernst law equation as follows:

$$E_{RHE} = E_{Ag/AgCl} + 0.21 + 0.059 \times pH$$

where $E_{RHE}$ is the potential of the RHE and $E_{Ag/AgCl}$ is the measured potential against the Ag/AgCl (3 M KCl) reference electrode. All electrodes were stored under ambient conditions and were characterized several days to weeks after electrode preparation. All electrochemical measurements were performed at room temperature.

## 3. Results and discussion

The morphology of N-doped amorphous Mo films was analyzed by SEM, revealing a dense columnar structure typical of 3D growth modes (Fig. 1). The film thickness is approximately 2 μm. This morphology, characterized by closely packed columns, is commonly observed in thin films that follow a 3D growth mode [15]. EDS mapping confirms the homogeneous distribution of Mo, uniform N-doping, and surface oxygen adsorption (Fig. 1, inset). The nitrogen present in the film originates from the use of $N_2$ during deposition. Under high laser fluence, reactive nitrogen species bond with Mo atoms ablated in the plasma plume, resulting in the formation of N-doped Mo films on the substrate. Since oxygen was not introduced during deposition, the observed oxygen is attributed to surface physisorption and the formation of a native oxide layer upon air exposure, particularly on the porous N-doped surface.

The morphology of amorphous N-doped Mo thin films deposited on carbon paper substrates is shown in Fig. 2(a1–a3). The carbon paper consists of a dense network of carbon fibers with diameters of approximately 10 μm. A macroscopic image of the sample is provided in Fig. S2. Fig. 2(a1–a3) presents SEM images of the as-deposited N-doped Mo thin films at varying magnifications. Each column is composed of clusters of nanoparticles. Due to the curved morphology of the carbon fibers and the 3D growth mode, micro- and nano-fissures appear between Mo columns. These features enhance the film's porosity and electrochemically active surface area, potentially improving the electrocatalytic performance of the nanocomposites. EDS maps of Mo $L_\alpha$ and N $K_\alpha$ confirm their uniform distribution along the carbon fiber surface. The microscopic features of the nanocomposites remain largely unchanged after annealing in an Ar atmosphere (Fig. 2(b1–b3)). Porosity, fissure dimensions, and particle clustering characteristics are similar to those of the pristine sample. The fissure-covered area, measured from top-view SEM images, decreases slightly from 45 % in the pristine sample to 39 % in the Ar-annealed sample. In contrast, annealing in a $CH_4$ atmosphere results in a more compact morphology and reduced fissure dimensions (Fig. 2(c1–c3)), with the fissure-covered area -of 16 % (Fig. S3). This compaction is likely due to enhanced carbon incorporation into the metallic lattice, leading to carburization.

The EDS of both pristine and annealed samples shows signals for Mo (2.3 eV), as well as C, O, and N (0.3–1 eV) (Fig. 3a). Raman spectra of the pristine and annealed Mo-based nanocomposites are shown in Fig. 3b. The spectrum of the pristine Mo sample exhibits peaks in the 100–1000 $cm^{-1}$ range. Major peaks appear at 121 $cm^{-1}$, 335 $cm^{-1}$, 816 $cm^{-1}$, and 981 $cm^{-1}$, corresponding to $MoO_2$ and $MoO_3$, which form upon air exposure [16,17]. The peak at 277 $cm^{-1}$ is assigned to the out-of-plane $A_1'$ mode, indicative of the $Mo_2N$ phase [18,19]. Raman characterization of the pristine sample, performed right after the deposition step, does not reveal the formation of an oxide phase (Fig. S4). The oxide formation is physiosorbed, which is completely due to the porous nature of the as-grown film. Nevertheless, Raman characterization performed on the same pristine sample (before exposure to annealing) weeks later, shows the presence of oxide phase (Fig. 3b, blue graph). For this, we conclude that long exposure to the atmosphere is required for the oxidation process to occur. During the high-temperature annealing process under the gaseous environment (CH4 and Ar), the surface absorbed oxygen is evaporated. After annealing in Ar or $CH_4$, oxide-related peaks disappear, indicating surface reduction. A new peak at ~140 $cm^{-1}$, attributed to the $A_{1g}^1$ mode of orthorhombic $Mo_2C$, emerges, while the nitride-related signal vanishes—suggesting successful formation of a stable carbide phase [20,21]. Annealed samples are resistant to oxidation. This implies that high-temperature annealing induces carburization in both Ar and $CH_4$ atmospheres. These findings are further supported by XRD and XPS analyses, discussed below. At the same time, surface graphitization due to methane pyrolysis is excluded, since graphitic Raman bands in the 1000–3000 $cm^{-1}$ region are not observed (Fig. S5).

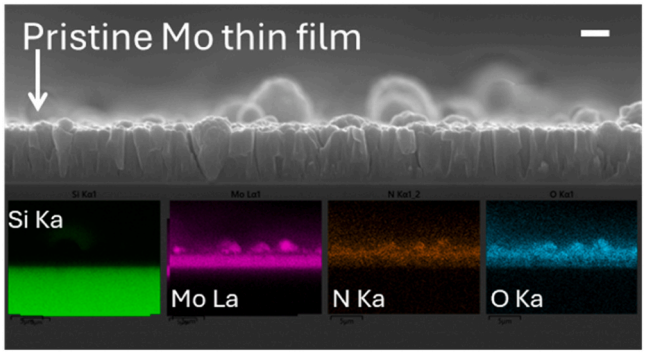


**Fig. 1.** Cross-sectional SEM image of the pristine Mo film deposited on Si (scale bar 1 μm). Inset: Energy-dispersive spectroscopy (EDS) mapping of Si Ka, Mo La, N Ka and O Ka.

XRD patterns of the pristine and annealed samples are presented in Fig. 3c. In the pristine sample, diffraction peaks from the Mo composite are observed at 36.9° ($MoO_2$, JCPDS 00–032–0671) and 40.4° (Mo, JCPDS 00–042–1120). Additionally, graphite peaks from the substrate appear at 26.3°, 42°, and 54.4° (graphite, JCPDS 01–075–2078). Peaks corresponding to $Mo_2N$ are located at 37.4° and 43.5° ($Mo_2N$, JCPDS 25–1366). Both annealed samples exhibit diffraction peaks at 34.4°, 37.9°, 39.4°, and 52.1°, which correspond to the orthorhombic $Mo_2C$ phase (JCPDS 00–011–0680). The metallic Mo peak remains distinct, while the oxide-related peak intensity is significantly reduced. The full width at half maximum (FWHM) of the main carbide peaks was measured for both Ar- and $CH_4$-annealed samples (Table 1). Using the Scherrer equation, the average crystallite size of $Mo_2C$ was calculated [22]. The FWHM values are nearly identical for both atmospheres, suggesting that the annealing environment has little effect on the crystallite size of the $Mo_2C$ phase.

The surface states of the pristine and annealed Mo composites were characterized by XPS (Fig. 4). The wide-scan spectra are shown in Fig. 4a. All spectra exhibit signals from Mo 3*d*, Mo 3*p*, C 1 *s*, O 1 *s*, and N 1 *s*. Comparison of the C 1 *s* spectra shows no significant shift in peak position. All C 1 *s* peaks are centered at 284.4 eV, indicating the presence of both C–C and C═C bonding. A carbide-related component—typically appearing as a shoulder at lower binding energies—is not observed in either the pristine or annealed samples. The FWHM of the C 1 *s* peak for the pristine sample (1.75 eV) is slightly larger than that of the annealed samples (1.56 eV), suggesting a reduction of C–O and C═O components upon annealing (Fig. S6). Significant modifications in the Mo 3*d* spectra are observed after annealing. The pristine sample exhibits peaks at 235.9 eV and 232.8 eV ($Mo^{6+}$, indicative of $MoO_3$), 232.9 eV and 229.8 eV ($Mo^{4+}$, $MoO_2$), and 233.9 eV and 230.8 eV ($Mo^{5+}$, MoN) (Fig. 4b). Deconvolution confirms the formation of N-doped $MoO_x$ (x = 2, 3), consistent with Raman and XRD results [23]. In annealed samples, a shoulder appears around 231.3 eV, attributed to Mo–C bonding and indicative of carburization. Additionally, a new peak at 228.3 eV confirms the formation of Mo carbide [24]. The deconvoluted Mo 3*d* spectrum for the sample annealed in Ar (Fig. 4c) shows components at 236.1 eV and 233.0 eV ($Mo^{6+}$, $MoO_3$), 232.8 eV and 229.7 eV ($Mo^{4+}$, $MoO_2$), 233.8 eV and 230.6 eV ($Mo^{5+}$, MoN), and 231.7 eV and 228.5 eV ($Mo^{2+}$, MoC). The spectrum for the $CH_4$-annealed sample (Fig. 4d) reveals the same components with variations in peak areas. The relative areas of $MoO_2$, $MoO_3$, MoN, and MoC for each sample are listed in Table S1. These data show that reduction is more pronounced in the methane-annealed sample, indicating enhanced $MoO_2$ reduction and carburization compared to the Ar-annealed sample [25]. The MoN peak area remains relatively unchanged between the pristine and Ar-annealed samples but decreases in the $CH_4$-annealed sample, possibly due to $NH_3$ formation. The MoC content is higher in the $CH_4$-annealed sample (14.4 %) compared to the Ar-annealed one

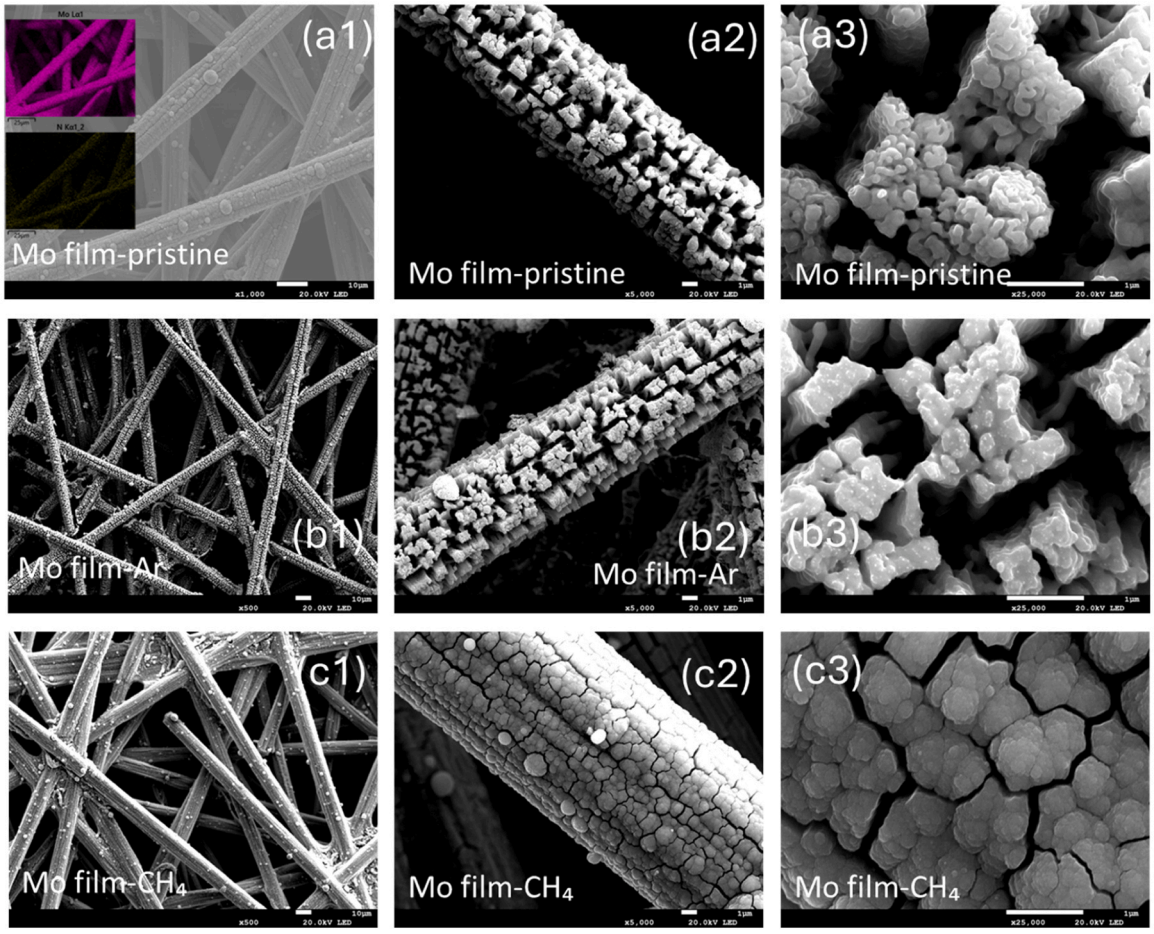


**Fig. 2.** SEM images of Mo composites deposited on carbon paper. A) As-deposited Mo thin films shown in varying magnifications, scale bars are 100 μm (a1) and 10 μm (a2 and a3), respectively. EDS maps of Mo and N (inset a1). B) Mo thin films annealed in Ar atmosphere, shown in varying magnifications, scale bars are 100 μm (b1) and 10 μm (b2 and b3), respectively. C) Mo thin films annealed in $CH_4$ atmosphere, shown in varying magnifications, scale bars are 100 μm (c1) and 10 μm (c2 and c3), respectively.

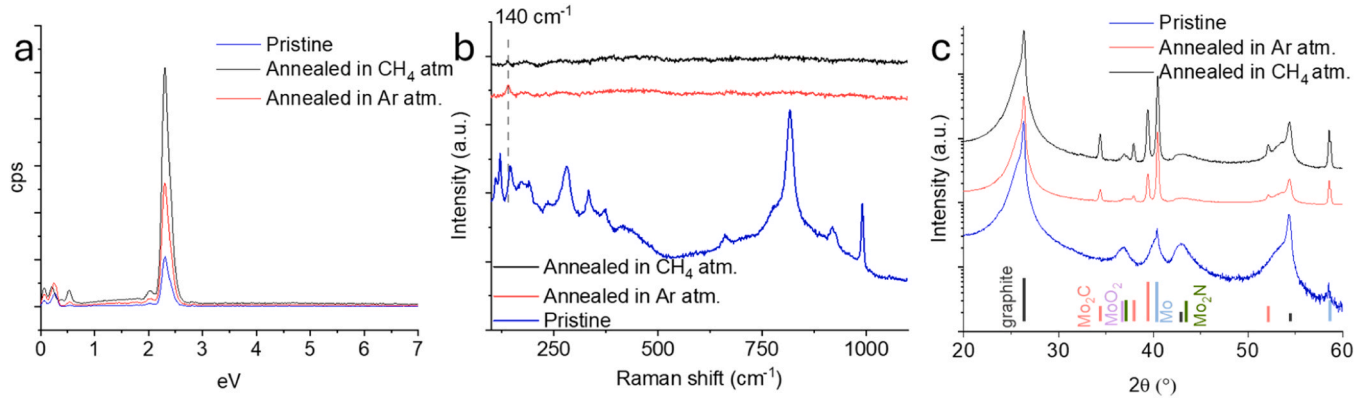


**Fig. 3.** a) EDS spectra of the pristine and annealed samples, b) Raman spectra of the pristine and annealed samples and c) XRD spectra of the pristine and annealed samples.

(12.5 %). Wide-scan spectra were also used to analyze N 1 *s* photoemission. A zoomed-in view is presented in Fig. S7. In the pristine sample, the N 1 *s* peak is centered at 397.6 eV, confirming Mo–N bond formation [26]. After annealing, a slight shift to ~398 eV is observed, attributed to the reduction of surface molybdenum oxides. Overall, XPS analysis confirms the formation of N-doped $Mo_2C$ as a result of high-temperature annealing.

A schematic illustration (Fig. 5) summarizes the annealing processes in Ar and $CH_4$ atmospheres, integrating findings from XRD and XPS analyses. Molybdenum nitride formation occurs during the PLD process. Nitrogen incorporation may occur at different stages of PLD: i) during target ablation, where nitrogen reacts with heated Mo atoms, resulting in the ablation of pre-nitrided material; ii) during plume transport, via high-energy collisions between Mo vapor and nitrogen molecules; iii) via thermally activated reactions at the growing film surface [27]. During annealing in an Ar atmosphere, the carbon substrate serves as the

**Table 1**
FWHM of x-ray diffraction peaks originating from the molybdenum carbide phase.

| Annealing atmosphere | FWHM of peak at 34.4° | FWHM of peak at 39.4° | FWHM of peak at 52.2° |
|---|---|---|---|
| $CH_4$ | 0.23 | 0.26 | 0.27 |
| Ar | 0.24 | 0.25 | 0.31 |

sole carbon source. Previous studies have shown that defective carbon nanostructures can supply carbon species that migrate and react with adjacent transition metals. This behavior has been observed in systems where Mo is deposited on graphene nanowalls [28] and carbon nanotubes [29]. In contrast, when Mo is deposited on graphitic, defect-free carbon, carburization does not occur. A Raman spectrum of the carbon paper substrate used in this study reveals a D peak centered at 1350 $cm^{-1}$ , indicative of structural defects in the graphite lattice. The G peak at 1582 $cm^{-1}$ confirms the graphitic nature of the substrate

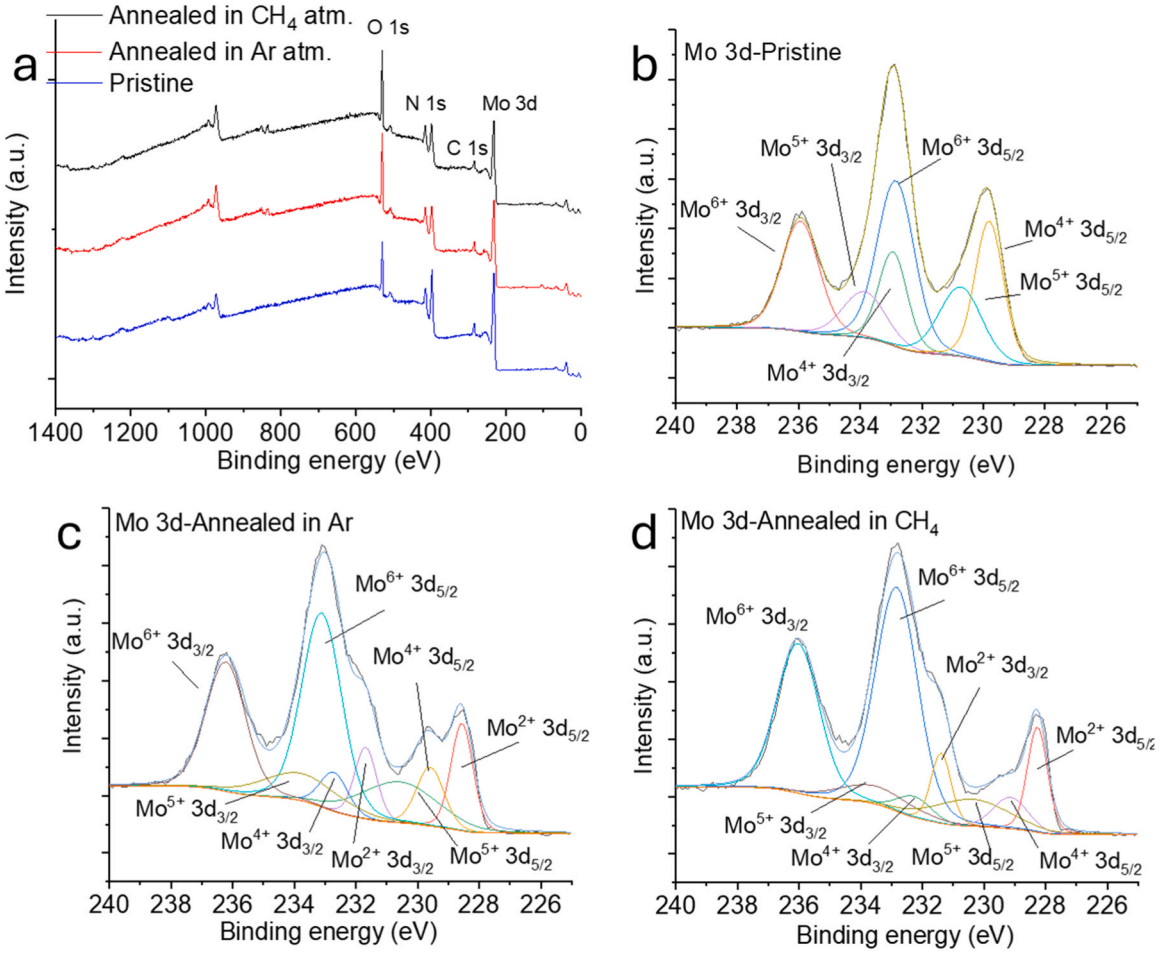


**Fig. 4.** XPS spectra of the pristine and annealed Mo composites: a) wide scan and Mo 3d of b) pristine, c) annealed in Ar atmosphere and d) annealed in $CH_4$ atmosphere.

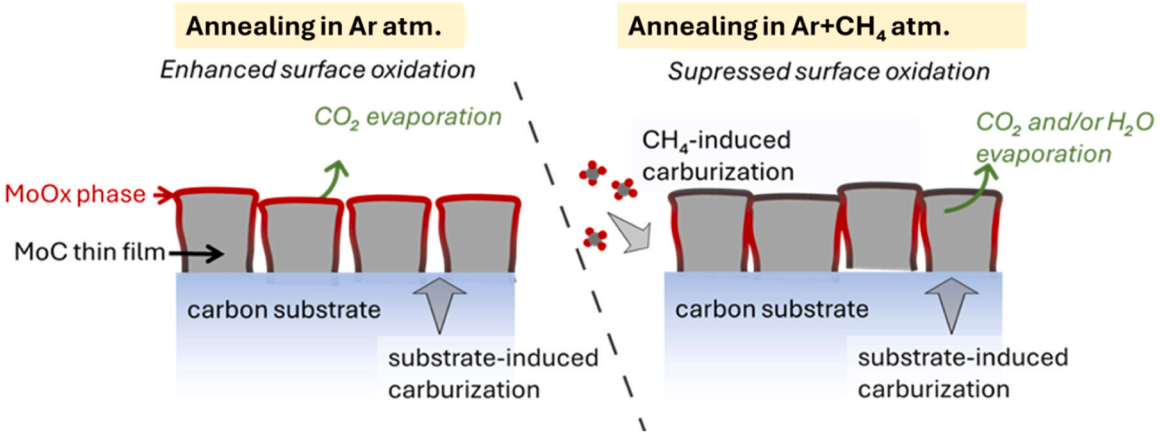


**Fig. 5.** Schematic illustration depicting the annealing step in argon and methane atmosphere.

(Fig. S8). These observations support the conclusion that the substrate contains defect sites that facilitate the migration of reactive carbon species, which in turn react with Mo and O, inducing the carburization of the first. Concurrently, molybdenum oxide reduction occurs via $CO_2$ evaporation. During annealing in Ar, carbon migrates and reacts with the metal at the substrate–metal interface, which may explain the slightly higher surface oxidation observed in these samples, as detected by XPS (Fig. 4c). To isolate the effect of the carbon substrate, a control sample with Mo deposited on Si was annealed under identical conditions, in Ar atmosphere. XRD analysis of this sample shows predominant formation of $MoO_2$ and Mo. A weak $Mo_2C$ peak at 39.8° is also present but is significantly lower in intensity compared to that observed in samples annealed on carbon substrates (Fig. S9a). This suggests that limited carburization may occur due to trace carbon, but it is far less efficient than when a carbon substrate is used. Annealing of Mo deposited on Si in a $CH_4$ atmosphere reveals the formation of carbide phases, evident by the rise of diffraction peaks at 32.9°, 39.9° and 49.5°. This finding confirms the role of methane in providing carbon species that assist Mo carburization (Fig. S9b). In the $CH_4$-annealed samples, both the carbon substrate and methane gas serve as carbon precursors. High temperature $CH_4$ pyrolysis results in the production of hydrogen, which reacts with oxygen present in the molybdenum surface, and the carbon species, which react with the Mo nanostructure. Thus, in this case, the carburization occurs via two pathways: the substrate–metal interface and the gas–metal surface interface. At the same time, Mo oxide reduction in this case proceeds via $CO_2$ and $H_2O$ evaporation—a process commonly known as methane steam reforming [30]—which also contributes to the suppression of surface oxidation.

The pristine and annealed samples were tested as cathode electrodes for water splitting to evaluate their electrocatalytic efficiency toward the hydrogen evolution reaction (HER). The LSV curves are shown in Fig. 6a. The pristine sample exhibits negligible current density within the examined voltage window, indicating that it requires a more negative onset potential to initiate HER. This behavior is attributed to the presence of oxide phases, which are less catalytically active and passivate the Mo surface.

The sample annealed in argon shows an onset potential of $\eta_o = -164$ mV vs. RHE and an overpotential at 10 mA cm$^{-2}$ ($\eta_{10}$) of −215 mV *vs.* RHE. In contrast, the sample annealed in methane demonstrates improved performance, with $\eta_o = -139$ mV *vs.* RHE and $\eta_{10} = -192$ mV *vs.* RHE. Tafel slope analysis was performed to evaluate the reaction kinetics of each sample (Fig. 6b). The Ar-annealed sample exhibits a Tafel slope of 84 mV dec$^{-1}$, while the $CH_4$-annealed sample shows a lower value of 73 mV dec$^{-1}$, indicating faster HER kinetics. These results confirm that the sample annealed in a methane atmosphere requires less applied energy to drive HER and achieves higher reaction rates. This improvement is attributed to enhanced crystallinity, increased electrical conductivity, and more effective reduction and carburization of the Mo surface. The durability of the $CH_4$-annealed sample—the most efficient catalyst—was evaluated using chronoamperometry. A constant potential of −290 mV *vs.* RHE was applied over 20 h. After approximately 1 h, the current density stabilized at ~30 mA cm$^{-2}$, and after 20 h, it remained at ~23 mA cm$^{-2}$, indicating excellent long-term stability. The ability to sustain moderate current density under continuous operation in acidic media demonstrates the nanocomposite's potential for industrial HER applications [31].

Cyclic voltammetry (CV) was performed to estimate the electrochemical double-layer capacitance ($C_{dl}$), which correlates with the electrochemically active surface area. The CV curves are shown in Fig. S10. $C_{dl}$ was extrapolated from the linear relationship between the current density ($I_{max}$) and scan rate. The Ar-annealed sample exhibits a $C_{dl}$ of 2.1 mF cm$^{-2}$, while the $CH_4$-annealed sample shows a ~3.3-fold increase with a $C_{dl}$ of 6.9 mF cm$^{-2}$. The higher capacitance reflects a larger electrochemically active surface area, which contributes to improved HER performance (Fig. 7a). EIS was also conducted to evaluate and compare the charge transfer resistance ($R_{ct}$) of the pristine and annealed samples. The Nyquist plots are presented in Fig. 7b. All samples exhibit semicircular profiles, indicative of a charge transfer process governed by interfacial kinetics at the electrode–electrolyte interface. A smaller semicircle diameter corresponds to lower $R_{ct}$ and thus better charge transfer efficiency. Among the three samples, pristine Mo shows the highest $R_{ct}$, followed by the Ar-annealed sample. The $CH_4$-annealed sample exhibits the lowest $R_{ct}$, confirming its superior interfacial charge transfer characteristics. Together, the CV and EIS analyses validate the enhanced electrocatalytic performance of the $CH_4$-annealed Mo composite, which combines a high electrochemical surface area with efficient charge transfer.

Finally, the HER performance of the N-doped $Mo_2C$ thin films was benchmarked against other planar $Mo_2C$-based composites by comparing $\eta_{10}$ values [25, 32–35] (Table 2). In addition, the present nanocomposite exhibits one of the highest reported activities when compared to carburized Mo films [36–37]. This superior performance is attributed to the synergistic effects of N-doping and the columnar film growth, which promotes the nanostructuring and crack formation. These structural features significantly increase the electrocatalytically active surface area.

The sample subjected to the chronoamperometry test was further examined by SEM, XPS, and XRD to assess its structural and morphological stability. SEM imaging confirms that the morphology of the sample remains unchanged after long-term operation, indicating strong adhesion of the Mo thin film to the carbon fiber surface (Fig. 8a). XPS analysis of the Mo 3*d* region reveals peaks centered at 235.6 eV and 232.5 eV, corresponding to $Mo^{6+}$ oxidation states, indicating surface oxidation (Fig. 8b). $Mo_2C$ oxidation occurs because of the prolonged exposure of Mo in the electrolyte solution, composed of sulfuric acid and water. Oxygen molecules or oxygen-containing anions possibly react with the Mo surface, leading to its oxidation. Nevertheless, we consider that this oxidation is limited to the $Mo_2C$ surface, in agreement with

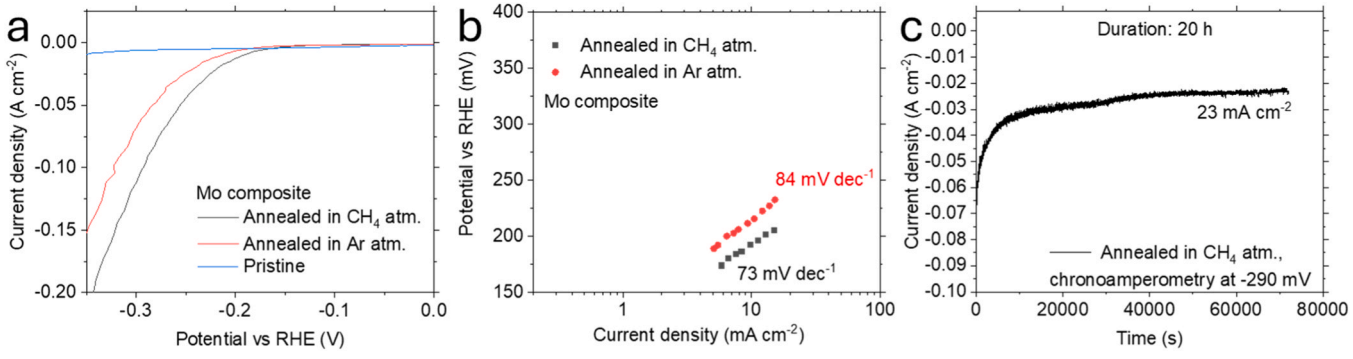


**Fig. 6.** LSV curves of pristine Mo (blue), Mo annealed in Ar atm. (red), and Mo annealed in methane atm. (black), (b) Tafel slopes produced from the LSVs, for the annealed samples c) Chronoamperometry test during 20 h under −290 mV continuous bias.

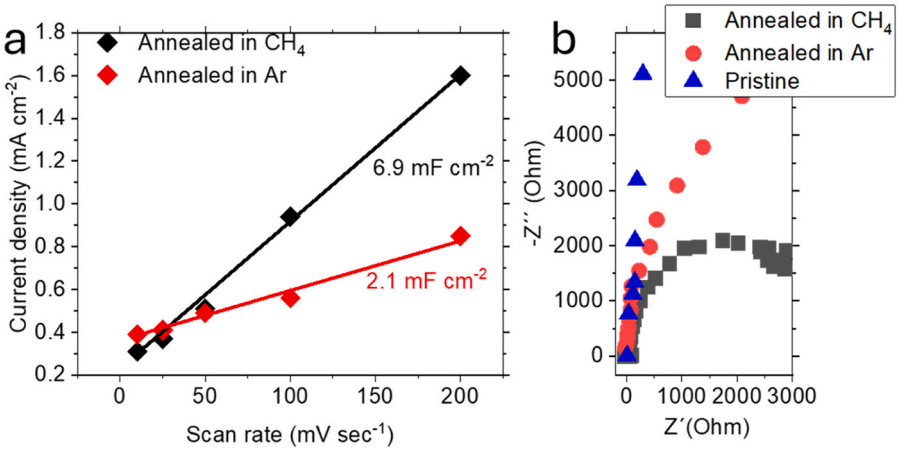


**Fig. 7.** a) Plot of current density with respect to scan rates applied during CV for Mo composites annealed in Ar and $CH_4$ atmosphere, b) Nyquist plots of the pristine and annealed Mo composites applying a potential of −500 mV vs Ref. electrode.

**Table 2**
Comparison of HER performance of different Mo-based nanostructures.

| Composite | Synthesis method | $\eta_{10}$ (mV) | Reference |
|---|---|---|---|
| N-doped $Mo_2C$ thin film | PLD+ annealing under $CH_4$ tm. | −192 | **Present work** |
| Chemical conversion of Mo to $Mo_2C$ | CVD in Cu vapor atm. | −270 | [32] |
| $Mo_2C$ Nanocrystals on Mo foil | Heat treatment under CO | −255 | [33] |
| $Mo_2C$ Hexagonal 2D domains | CVD on liquid Cu-Mo alloy | −270 | [34] |
| $Mo_2C$ nanocrystals | Amine-metal oxide composite carbothermic reduction | −325 | [35] |
| $Mo_2C$ anchored on graphene nanowalls | Impregnation in $MoCl_5$ precursor and carburization | −141 | [25] |

previous reports [33], leaving the underlying carbide phase untacked. This explains the prolonged electrocatalytic stability observed during chronoamperometry tests. EDS characterization further confirms the absence of contamination during testing; no additional elements were detected, aside from sulfur (S), which originates from the electrolyte (Fig. 8c). Overall, the post-chronoamperometry characterization demonstrates the morphological and chemical stability of the Mo-based composite under prolonged HER operation.

## 4. Conclusions

N-doped Mo thin films were successfully deposited on graphitic substrates via pulsed laser deposition in a nitrogen-rich atmosphere and subsequently converted into N-doped $Mo_2C$ through high-temperature annealing in Ar and $CH_4$ atmospheres. Crystallization and carburization of the N-doped Mo films occurred under both conditions, as confirmed by XRD analysis, highlighting the role of the carbon substrate as an effective carbon source for Mo carburization. Notably, XPS results indicate more efficient Mo oxide reduction and enhanced carburization in the $CH_4$ atmosphere, correlating with the superior electrocatalytic performance observed for this sample. The formation of Mo–N bonds confirms successful nitrogen doping of the $Mo_2C$ composite. The N-doped $Mo_2C$ thin films demonstrated one of the highest HER activities reported for planar $Mo_2C$-based catalysts, with an overpotential $\eta_{10} = -192$ mV vs. RHE for the sample annealed in methane.

This study demonstrates a simple and effective route for synthesizing N-doped nanostructured $Mo_2C$ thin films via high-temperature annealing, without the need for hazardous precursors such as $NH_3$. Furthermore, it reveals the critical role of the carbon substrate not only as a physical support but also as a reactive carbon source during carburization. These insights contribute to the broader understanding of metal carbide formation on carbon supports and offer a promising strategy for designing advanced electrocatalysts for sustainable energy applications.

## CRediT authorship contribution statement

**Stefanos Chaitoglou:** Writing – original draft, Investigation, Funding acquisition, Formal analysis, Data curation, Conceptualization. **Subrata Ghosh:** Writing – original draft, Investigation, Funding acquisition, Formal analysis, Conceptualization. **Shubhadeep Majumdar:** Investigation, Formal analysis, Data curation. **Roger Amade-Rovira:** Supervision, Resources, Project administration, Funding acquisition.

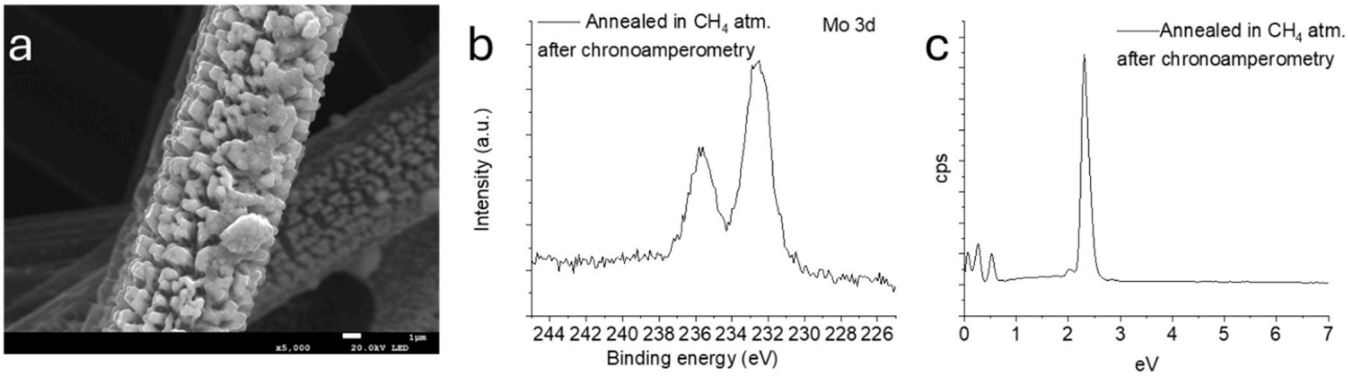


**Fig. 8.** a) SEM image, b) XPS spectrum in the Mo 3d energy region and c) EDS spectrum of the composite after tested via chronoamperometry.

**Enric Bertran-Serra:** Writing – original draft, Supervision, Resources, Project administration, Investigation. **Carlo S. Casari:** Supervision, Resources, Methodology, Investigation, Funding acquisition.

## Declaration of Competing Interest

The authors declare that they have no known competing financial interests or personal relationships that could have appeared to influence the work reported in this paper.

## Acknowledgements

The authors are grateful for the financial support provided by the Generalitat de Catalunya through the AGAUR grant for Project No. 2023 CLIMA 00009, with the support of the Department of Research and Universities: the Department of Climate Action, Food and Rural Agenda; and the Climate Fund of the Generalitat de Catalunya. The authors would like to thank the CCiT (Scientific and Technological Center)-UB for access to the structural and morphological characterization facilities. S.C. acknowledges support from the MSCA fellowship funded by the European Commission through grant agreement 101062014 (HORIZON Europe-MSCA-2021-PF-01). S.G. acknowledges Horizon Europe (HORIZON) for the Marie Sklodowska-Curie Fellowship (grant no. 101067998-ENHANCER). S. M. acknowledges the support from the predoctoral fellowship awarded by the Department of Research and Universities of the Generalitat de Catalunya, through the FISDUR program and co-financed by The European Social Fund Plus (file number 2024 FISDU 00010).

## Appendix A. Supporting information

Supplementary data associated with this article can be found in the online version at doi:10.1016/j.mtcomm.2025.114274.

## Data availability

Data will be made available on request.

## References

[1] A. Boretti, B.G. Pollet, Hydrogen economy: paving the path to a sustainable, low-carbon future, Int. J. Hydrog. Energy 93 (2024) 307–319.
[2] J. Li, W. Xie, H. Zhou, Z. Li, M. Shao, Techno-economic analysis of electrochemical hydrogen production coupled with alternative oxidation, Chem. Eng. Sci. 298 (2024) 120322.
[3] P. Quaino, F. Juarez, E. Santos, W. Schmickler, Volcano plots in hydrogen electrocatalysis – uses and abuses, S. Beilstein J. Nanotechnol. 5 (2014) 846–854.
[4] J.R. Kitchin, J.K. Nørskov, M.A. Barteau, J.G. Chen, Trends in the chemical properties of early transition metal carbide surfaces: a density functional study, Catal. Today 105 (2005) 66–73.
[5] Q. Gao, W. Zhang, Z. Shi, L. Yang, Y. Tang, Structural design and electronic modulation of transition-metal-carbide electrocatalysts toward efficient hydrogen evolution, Adv. Mater. 31 (2019) 1802880.
[6] X. Zou, H. Tang, J. Li, G. Gao, Z. Geng, L. Li, G. Li, Phase-controlled synthesis of starch- derived $Mo_2C$–MoC/C heterostructure catalyst for electrocatalytic hydrogen evolution reaction, Int. J. Hydrog. Energy 79 (2024) 525–536.
[7] R.A. Mir, S. Upadhyay, O. Pandey, A review on recent advances and progress in $Mo_2C$@C: a suitable and stable electrocatalyst for HER, Inter. J. Hydrog. Energy 48 (2023) 13044–13067.
[8] S. Chaitoglou, S. Ghosh, R. Ospina, Y. Ma, R. Amade-Rovira, C.S. Casari, E. Bertran-Serra, Tungsten carbide nanoparticles embedded in carbon nanofoam composites for efficient electrocatalytic hydrogen evolution, Adv. Energy Sustain. Res. (2025) 2500016.
[9] R. Teghil, A.De Bonis, A. Galasso, M. Sansone, J.V. Rau, A. Santagata, Nanostructured molybdenum carbide thin films obtained by femtosecond pulsed laser deposition, Phys. Status Solidi C (2012) 2370–2373.
[10] Y. Huang, J. Ge, J. Hu, J. Zhang, J. Hao, Y. Wei, Nitrogen-doped porous molybdenum carbide and phosphide hybrids on a carbon matrix as highly effective electrocatalysts for the hydrogen evolution reaction, Adv. Energy Mater. 6 (2018) 1701601.
[11] H. Wei, J. Wang, Q. Lin, Y. Zou, X. Chen, H. Zhao, J. Li, H. Jin, Y. Lei, S. Wang, Incorporating ultra-small N-doped $Mo_2C$ nanoparticles onto 3D N-doped flower-like carbon nanospheres for robust electrocatalytic hydrogen evolution, Nanomater Energy 86 (2021) 106047.
[12] Q. Jing, J. Zhu, X. Wei, Y. Lin, X. Wang, Z. Wu, An acid-base molecular assembly strategy toward N-doped $Mo_2C$@C nanowires with mesoporous $Mo_2C$ cores and ultrathin carbon shells for efficient hydrogen evolution, S. J. Colloid Interface Sci. 602 (2021) 520–533.
[13] Q. Li, Y. Hou, N. Xiang, Y. Liu, Z. Huang, A new insight into the promotional effect of nitrogen-doping in activated carbon for selective catalytic reduction of $NO_X$ with $NH_3$, Sci. Total Environ. 740 (2020) 140158.
[14] S. Ghosh, M. Righi, A. Macrelli, F. Goto, V. Russo, A.L. Bass, C.S. Casari, Low-density functionalized amorphous carbon nanofoam as binder-free Thin-film Supercapacitor electrode, Carbon Trends 20 (2025) 100516.
[15] A. Macrelli, M. Olivieri, A. Lamperti, V. Russo, B. Bozzini, M. Menegazzo, G. Bussetti, C.S. Casari, A.Li Bassi, Nanostructured $ZnxMn_{3-x}O_4$ thin films by pulsed laser deposition: a spectroscopic and electrochemical study towards the application in aqueous Zn-ion batteries, Electrochim. Acta 442 (2023) 141909.
[16] M. Mestl, G. Dieterle, Raman spectroscopy of molybdenum oxides, Phys. Chem. Chem. Phys. 4 (2002) 822–826.
[17] M.A. Camacho-López, L. Escobar-Alarcón, M. Picquart, R. Arroyo, G. Córdoba, E. Haro-Poniatowski, Micro-Raman study of the m-$MoO_2$ to a-$MoO_3$ transformation induced by cw-laser irradiation, Opt. Mater. 33 (2011) 480.
[18] H. Xu, C. Gao, L. Kong, D. Li, J. Lin, Constructing hierarchical porous $MoO_2$@ $Mo_2N$@C composite via a confined pyrolysis synthetic strategy towards lithium-ion battery anodes, Chem. Eur. J. 29 (2023) e202301565.
[19] C.-H. Yao, H. Gao, L. Ping, D.P. Gulo, H.-L. Liu, N.T. Hung, R. Saito, X. Ling, Nontrivial Raman characteristics in 2D Non-Van der Waals $Mo_5N_6$, ACS Nano 18 (2024) 32458–32467.
[20] S. Chaitoglou, P. Tsipas, T. Speliotis, G. Kordas, A. Vavouliotis, A. Dimoulas, Insight and control of the chemical vapor deposition growth parameters and morphological characteristics of graphene/$Mo_2C$ heterostructures over liquid catalyst, J. Cryst. Growth 495 (2018) 46–53.
[21] S. Chaitoglou, T. Giannakopoulou, T. Speliotis, A. Vavouliotis, C. Trapalis, A. Dimoulas, $Mo_2C$/graphene heterostructures: low temperature chemical vapor deposition on liquid bimetallic Sn–Cu and hydrogen evolution reaction electrocatalytic properties, Nanotechnology 30 (2019) 125401.
[22] L.S. Macedo, R.R. Oliveira Jr., T. van Haasterecht, V. Teixeira da Silva, H. Bitter, Influence of synthesis method on molybdenum carbide crystal structure and catalytic performance in stearic acid hydrodeoxygenation, Appl. Catal. BEnviron. 241 (2019) 81–88.
[23] X. Pan, B. Xi, H. Lu, Z. Zhang, X. An, J. Liu, J. Feng, S. Xiong, Molybdenum oxynitride atomic nanoclusters bonded in nanosheets of N-doped carbon hierarchical microspheres for efficient sodium storage, NanoMicro Lett. 14 (2022) 163.
[24] S. Chaitoglou, R. Ospina, E. Bertran-Serra, Cluster $Mo_2C$ deposited on graphene nanowalls by x-ray photoelectron spectroscopy, Surf. Sci. Spectra 31 (2024) 014001.
[25] S. Chaitoglou, R. Ospina, Y. Ma, R. Amade, X. Vendrell, J. Rodriguez-Pereira, E. Bertran-Serra, Deposition and in-situ formation of nanostructured $Mo_2C$ nanoparticles on graphene nanowalls support for efficient electrocatalytic hydrogen evolution, J. Alloy. Compd. 972 (2024) 172891.
[26] J. Jia, T. Xiong, L. Zhao, F. Wang, H. Liu, R. Hu, J. Zhou, W. Zhou, S. Chen, Ultrathin N-doped $Mo_2C$ nanosheets with exposed active sites as efficient electrocatalyst for hydrogen evolution reactions, ACS Nano 11 (2017) 12509–12518.
[27] M. Bereznai, Z. Tóth, A.P. Caricato, M. Fernandez, A. Luches, G. Majni, P. Mengucci, P.M. Nagy, A. Juhasz, L. Nanai, Reactive pulsed laser deposition of thin molybdenum- and tungsten-nitride films, Thin Solid Films 473 (2005) 16–23.
[28] S. Chaitoglou, R. Amade, R. Ospina, E. Bertran-Serra, Hybrid nanostructured compounds of $Mo_2C$ on vertical graphene nanoflakes for a highly efficient hydrogen evolution reaction, ACS Appl. Energy Mater. 6 (2023) 6120–6131.
[29] S. Majumdar, S. Chaitoglou, J. Serafin, G. Farid, R. Ospina, Y. Ma, R. Amade-Rovira, E. Bertran-Serra, Enhancing hydrogen evolution: carbon nanotubes as a scaffold for $Mo_2C$ deposition via magnetron sputtering and chemical vapor deposition, Inter. J. Hydrog. Energy 89 (2024) 977–989.
[30] T. Christofoletti, J.M. Assaf, E.M. Assaf, Methane steam reforming on supported and non-supported molybdenum carbides, Chem. Eng. J. 106 (2005) 97–103.
[31] T. Wu, M. Sun, H.H. Wong, C.H. Chan, L. Lu, Q. Lu, B. Chen, B. Huang, Recent advances and strategies of electrocatalysts for large current density industrial hydrogen evolution reaction, Inorg. Chem. Front 10 (2023) 4632–4649.
[32] S. Chaitoglou, T. Giannakopoulou, G. Papanastasiou, D. Tsoutsou, A. Vavouliotis, C. Trapalis, A. Dimoulas, Cu vapor-assisted formation of nanostructured $Mo_2C$ electrocatalysts via direct chemical conversion of Mo surface for efficient hydrogen evolution reaction applications, Appl. Surf. Sci. 510 (2020) 145516.
[33] J.S. Kang, J. Kim, M.J. Lee, Y.J. Son, D.Y. Chung, S. Park, J. Jeong, J.M. Yoo, H. Shin, H. Choe, H.S. Park, Y.E. Sung, Electrochemically synthesized nanoporous molybdenum carbide as a durable electrocatalyst for hydrogen evolution reaction, Adv. Sci. 5 (2018) 1700601.
[34.] Y. Yin, C. Xu, Z. Liu, W. Ren, C. Sun, Ultrathin α-$Mo_2C$ dominated by (100) Surface/Cu Schottky junction as efficient catalyst for hydrogen evolution, Int. J. Hydrog. Energy 44 (2019) 853–859.
[35] Y.N. Regmi, C. Wan, K.D. Duffee, B.: M. Leonard, Nanocrystalline $Mo_2C$ as a bifunctional Water Splitting Electrocatalyst, ChemCatChem 7 (2015) 3911-3915.
[36] L. Jin, Z. Pan, L. Wang, X. Ji, Effect of thermal annealing on phase structure and hydrogen evolution reaction of molybdenum carbide thin films prepared by co-sputtering, Thin Solid Films 809 (2025) 14.
[37] X. Cao, A. Jiang, S. Tao, J. Liu, J. Xiao, Structure and electrocatalytic hydrogen evolution performance of $Mo_2C$ thin films prepared by magnetron sputtering, Int. J. Hydrog. Energy 48 (2023) 24196–24206.